

pubs.acs.org/JACS Article

Spectroscopic Definition of a Highly Reactive Site in Cu-CHA for Selective Methane Oxidation: Tuning a Mono- μ -Oxo Dicopper(II) Active Site for Reactivity

Hannah M. Rhoda,^{\$} Dieter Plessers,^{\$} Alexander J. Heyer, Max L. Bols, Robert A. Schoonheydt,^{*} Bert F. Sels,^{*} and Edward I. Solomon^{*}



Cite This: J. Am. Chem. Soc. 2021, 143, 7531–7540



ACCESS

Metrics & More

Article Recommendations

Supporting Information

ABSTRACT: Using UV–vis and resonance Raman spectroscopy, we identify a $[Cu_2O]^{2+}$ active site in O_2 and N_2O activated Cu-CHA that reacts with methane to form methanol at low temperature. The Cu–O–Cu angle (120°) is smaller than that for the $[Cu_2O]^{2+}$ core on Cu-MFI (140°) , and its coordination geometry to the zeolite lattice is different. Site-selective kinetics obtained by operando UV–vis show that the $[Cu_2O]^{2+}$ core on Cu-CHA is more reactive than the $[Cu_2O]^{2+}$ site in Cu-MFI. From DFT calculations, we find that the increased reactivity of Cu-CHA is a direct reflection of the strong $[Cu_2OH]^{2+}$ bond formed along the H atom abstraction reaction coordinate. A systematic evaluation of these $[Cu_2O]^{2+}$ cores reveals that the higher O–H bond strength in Cu-CHA is due to the relative orientation of the two planes

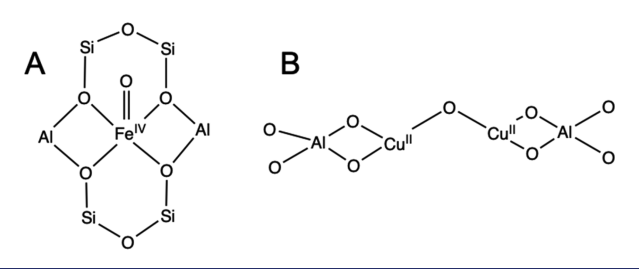
Energy 4

of the coordinating bidentate O-Al-O T-sites that connect the $[Cu_2O]^{2+}$ core to the zeolite lattice. This work along with our earlier study (J. Am. Chem. Soc, 2018, 140, 9236–9243) elucidates how zeolite lattice constraints can influence active site reactivity.

1. INTRODUCTION

The direct conversion of methane into methanol would have large advantages in industry, as current processes to produce methanol require harsh and expensive conditions. This onestep oxidation is difficult due to the strong C-H bond of CH₄ and the tendency for further oxidation of the methanol product. 1,2 In nature, the Cu- and Fe-enzymes particulate and soluble methane monooxygenase (pMMO and sMMO) catalyze this reaction at ambient conditions, but the nature of the active sites in these enzymes remains an open issue.³⁻ Cu- and Fe-doped zeolites also convert methane to methanol in the gas phase at relatively low temperatures.^{8–12} The iron active site, alpha-O, has been well-defined as a high-spin Fe(IV)=O site located in a 6-membered zeolite ring (Scheme 1A) and can react with methane at room temperature. 9,13 This alpha-O site is formed when the alpha-Fe precursor reacts with N₂O at 160 °C. 13 Whether alpha-O can be formed by O₂ and in what topologies is an open issue.¹⁴ In Cu zeolites, a variety of active sites have been proposed to hydroxylate methane $^{12,15-18}$ but only the $[\mathrm{Cu_2O}]^{2+}$ active sites in Cu-MFI and Cu-MOR (Scheme 1B) have been well-defined in terms of structure and reactivity.^{8,10} These [Cu₂O]²⁺ sites have the advantage of being generated with O2 in addition to N2O, however they are less reactive with CH4 than the alpha-O site in Fe-zeolites that can react at room temperature. Identifying a Cu/O active site that can react at a lower temperature would

Scheme 1. (A) Structure of alpha-O Site Located in a 6MR and (B) Structure of $[Cu_2O]^{2+}$ Site with Bidentate O-Al-O T-Site Coordination



be advantageous for potential applications in CH₄ conversion and abatement. 19

Copper-exchanged CHA zeolites have received significant research interest recently, both for their outstanding DeNOx capabilities, being commercialized for selective catalytic reduction (SCR) of NOx gases in heavy vehicles, ^{20–22} and for their partial methane oxidation performance. ²³ Cu-CHA

Received: March 16, 2021 Published: May 10, 2021

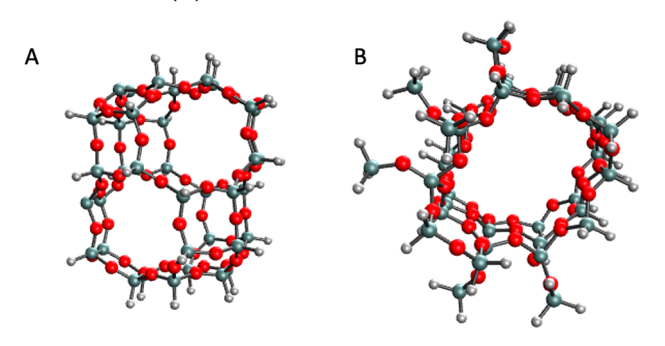




zeolites activated with either O_2 or N_2O can react with methane to form methanol at 200 °C. 15,16,24 With building on past studies on Cu-MFI 10 and Cu-MOR, 8,25 O_2 activated Cu-CHA has been studied by several groups using diffuse reflectance (DR-UV-vis-NIR) and resonance Raman (rR) spectroscopies. 15,16,26,27 This has led to various active site proposals and combinations thereof, including a trans- μ -1,2-peroxo dicopper(II) species ([CuOOCu] $^{2+}$), a mono- μ -oxo dicopper(II) species ([Cu2O] $^{2+}$), and Cu(II) superoxo species (both end-on and side-on). 15,16,26

Due to the simple structure with a unique T-site and its relevant applications, Cu-CHA is a model-system for understanding structure-activity relationships in zeolite catalysis, which makes a correct assignment of its active Cu site an important addition to the field.²³ To unambiguously determine the active site(s) responsible for methane activation in O₂ activated Cu-CHA, we performed an in-depth spectroscopic study. By collecting the rR excitation profile, extending the rR spectrum out to a higher energy region, identifying active site formation with N₂O, and using an ¹⁸O₂ perturbation of the rR vibrations, we elucidated the presence of a $[Cu_2O]^{2+}$ site that is different from the past assignments in Cu-CHA literature. 15,16 This $[Cu_2O]^{2+}$ also differs structurally from the one found in Cu-MFI, leading to higher methane activation reactivity $([Cu_2O]^{2+})$ in CHA is ~ 3 times more reactive than MFI at 25 °C). Using DFT, two contributions to reactivity were evaluated: the different contributions of physisorption in a Cu-CHA cage versus a 10MR channel in Cu-MFI (Scheme 2), and

Scheme 2. (A) Cage Structure in CHA Lattice with 8MR Windows and (B) 10MR Channel in MFI Lattice



the differences in the $[Cu_2O]^{2+}$ active site structure. Complementary to our earlier study on Cu-MOR where confinement increased physisorption and influenced reactiv-

ity, 25 the results here define a second means through which second sphere effects of the zeolite lattice contribute to reactivity. These structure—reactivity insights can help guide the engineering process toward materials with Cu/O active sites that exhibit higher reactivity, similar to alpha-O sites in Fe-zeolites. In combination with the advantage of using $\rm O_2$ as an oxidant in Cu-zeolites, this will broaden their potential applications.

2. RESULTS AND ANALYSIS

2.1. Physical Properties. Cu-CHA samples were prepared with Si/Al = 15.7 and Cu/Al = 0.29 (1.8 wt % Cu) according to the procedure in the Experimental Sections 1 and 2 in the SI. PXRD patterns of the calcined H–CHA materials as well as the Cu-CHA samples after Cu ion exchange (Experimental Section 2 in SI) and after a reaction cycle correspond to the standard pattern of pure, crystalline H–CHA zeolites with no large copper oxide clusters (Figure S1). The microporosity was determined by N_2 physisorption on calcined H–CHA (0.30 cm³/g) and Cu-CHA (0.28 cm³/g), in good agreement with literature (Figure S2). ¹⁵

2.2. DR–UV–vis–NIR Spectroscopy of Active Copper Site. DR–UV–vis–NIR spectra were measured after each sequential step in the activation procedure (Experimental Section 3 in SI). The DR–UV–vis–NIR spectra of Cu-CHA after calcination in O_2 flow at 450 °C, autoreduction in He flow at 700 °C, N_2O activation at 550 °C, and after CH_4 reaction at 200 °C (1 atm, 60 min) are shown in Figure 1A. Figure 1B shows the analogous cycle replacing N_2O with O_2 in the activation step.

After the calcination step, four Cu^{2+} d-d absorption bands can be distinguished at 11000, 13600, 16600, and 20000 cm⁻¹. These bands have often been observed in literature, $^{15,26-31}$ but an unequivocal assignment in terms of location or coordination of the Cu^{2+} has not yet been made.

After the autoreduction step in He at 700 $^{\circ}$ C, the intensity of the Cu²⁺ d-d bands was reduced, indicating that part of the Cu²⁺ was converted to Cu⁺. A similar autoreduction occurs in He at 500 $^{\circ}$ C (Figure S3).

Upon treatment with N_2O or O_2 at 550 °C, an absorption band appears around 22400 cm⁻¹, accompanied by a weaker absorption band around 6200 cm⁻¹. Both bands are more intense after N_2O than after O_2 . Similar 6200 and ~22000 cm⁻¹ absorption bands in Cu-MOR⁸ and Cu-MFI¹⁰ were assigned using rR spectroscopy and ¹⁸O perturbation to $[Cu_2O]^{2+}$ species that react with methane to form methanol. A

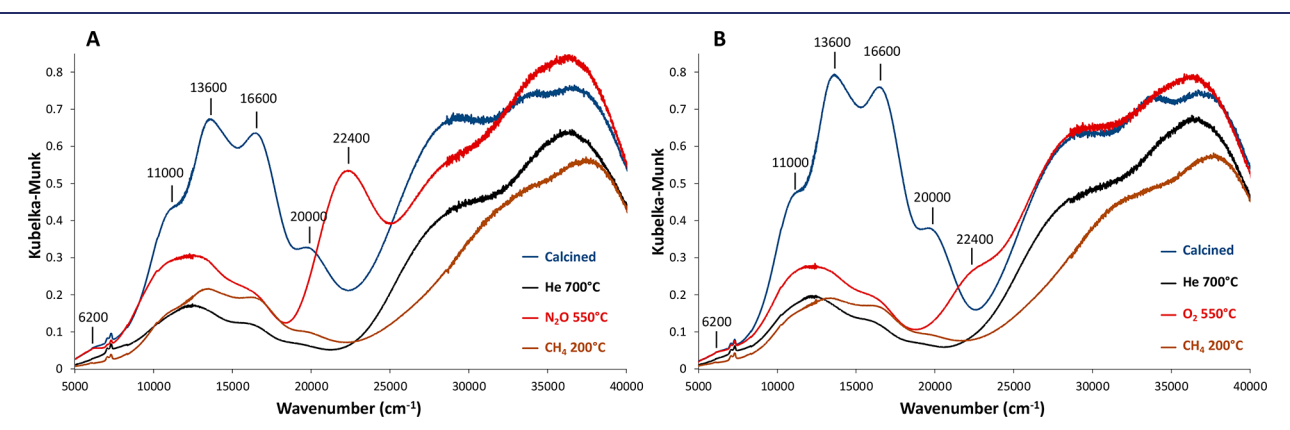


Figure 1. DR-UV-vis-NIR spectra after each step of a typical Cu-CHA activation cycle with (A) N₂O as the oxidant and (B) O₂ as the oxidant.

linear relationship between the intensity of this absorption band and methanol production was previously obtained for Cu-MFI.³²

The 22400 cm⁻¹ band disappears after 60 min of exposure to methane at 200 °C (Figure 1), but not in Helium (Figure S4), indicating a reaction with methane. Liquid extraction (see Experimental Section 4 in the SI) recovers 82.2 µmol methanol/g for N₂O activated Cu-CHA and 63.6 μmol methanol/g for O2 activated Cu-CHA. The molar methanol/ Cu ratios are 0.29 and 0.22, respectively, for N₂O and O₂ activation, comparable to the largest values reported in literature. 16 Absorption bands around 28100 cm^{-1} and 35300 cm^{-1} were also lost in the CH_4 reaction step (See UV-vis difference spectra in Figure S5). Both have been linked to methanol production in literature; 15,27,28 however, their decay does not correlate with that of the 22400 cm⁻¹ band and they were already present after He 700 °C, suggesting they represent different sites. Methane reaction immediately after He 700 °C (no O₂ or N₂O activation) recovers 25.0 μ mol methanol/g, which we attribute to the copper species related to the 28100 cm⁻¹ and 35300 cm⁻¹ absorption bands (Figure 1). Similar methanol production of autoreduced Cu-zeolites after reaction with CH4 has been observed in other systems. 15,33,34

2.3. Spectroscopic Definition of the Active Copper **Site.** Laser excitation into the 22400 cm⁻¹ absorption feature resonantly enhances similar vibrations in both the N₂O and O₂ activated Cu-CHA that are not observed after the autoreduction step (Figure 2). Like the 22400 cm⁻¹ band, these are not present before activation and are eliminated upon reaction with methane (Figure S6). The vibrations resonantly enhanced in the N₂O activated Cu-CHA sample (Figure 2, middle) are identical to those enhanced in the O2 activated Cu-CHA sample (Figure 2, bottom). The vibrations are more intense in

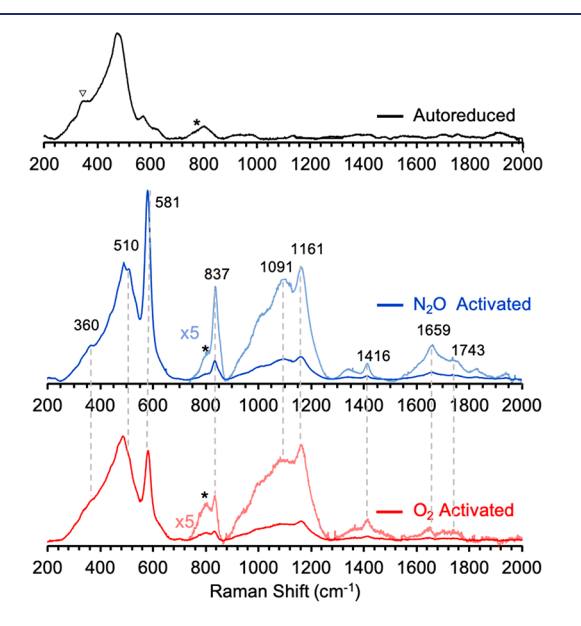


Figure 2. Comparison of the resonance Raman spectra ($\lambda_{ex} = 458$ nm) of autoreduced (top black), N2O activated (middle blue), and O2 activated (bottom red) Cu-CHA. The features that are resonantly enhanced are identified by the dotted lines (* indicates a feature from the glass sample holder, ∇ indicates a lattice feature in the autoreduced sample). The rR spectrum of H-CHA can be found in SI Figure 7 for reference.

the N₂O activated sample consistent with the more intense 22400 cm⁻¹ band in the N₂O activated Cu-CHA in Figure 1A. Thus, the same species is formed upon activation of the autoreduced zeolite with either O2 or N2O. Scanning the rR laser lines along the 22400 cm⁻¹ chromophore demonstrates that all these vibrations profile with the 22400 cm⁻¹ absorbance indicating that all the vibrations are associated with the same species (Figure 3).

The most intense Raman feature in Figure 2 at 581 cm⁻¹ is found to be ${}^{18}O_2$ isotope sensitive $(\Delta({}^{18}O_2) = 21 \text{ cm}^{-1}; \text{ see}$ Figure S8) as well as the features at 837 cm⁻¹ (Δ (¹⁸O₂) = 43 cm⁻¹) and 1161 cm⁻¹ (Δ (¹⁸O₂) = 32 cm⁻¹). No other isotope shifts were observed above noise due to the lower Raman intensity of O2 activated Cu-CHA and an incomplete labeling with $^{18}O_{2}$.

Cu-MFI and Cu-MOR stabilize [Cu₂O]²⁺ cores that can be formed with both O2 and N2O and exhibit similar rR features that are associated with their ~22000 cm⁻¹ absorbance bands.^{8,10} On the basis of this similarity, the most intense feature at 581 cm⁻¹ (Δ (¹⁸O₂) = 21 cm⁻¹) is assigned as the symmetric stretch of an oxo group bridging two Cu centers and the vibration at 837 cm⁻¹ is assigned as the oxo antisymmetric stretch. This assignment is validated by the observation of progressions in the region between 1000 cm⁻¹ and 2000 cm⁻¹ (Figure 2). The second and third quanta of the 581 cm⁻¹ symmetric stretch are observed at 1161 and 1743 cm⁻¹, respectively. The second member of a progression in the 837 cm⁻¹ antisymmetric vibration is observed at 1659 cm⁻¹. The 360 cm⁻¹ vibration is assigned as a Cu-O-Cu bend vibration. Finally, the tetrahedral site (T-site) ligand shows a resonance enhanced vibration at 510 cm⁻¹ (no isotope perturbation), and this forms a combination band with the symmetric stretch (581 cm⁻¹) at 1091 cm⁻¹.

Our assignment of the rR features of the Cu-CHA active site is different from those previously proposed in the literature. The features at 581 and 837 cm⁻¹ were previously assigned as the Cu–O stretch and the O–O stretch of a trans- μ -1,2-peroxo species, respectively. Trans- μ -1,2-peroxo species have been extensively defined in the literature and do indeed have Cu-O stretches between 550 and 600 cm⁻¹ and O-O stretches between 800 and 850 cm⁻¹.35-38 However, due to the nature of the charge transfer (CT) transition responsible for the resonance enhancement in trans- μ -1,2-peroxo bridged Cu(II)₂ sites, the O–O stretch is more intense than the Cu–O stretch; this intensity pattern is opposite to that experimentally observed in Cu-CHA. The 837 cm⁻¹ feature is weak and now assigned as an antisymmetric stretch which is not rR allowed in idealized Cu₂O C_{2V} symmetry and the 581 cm⁻¹ feature is intense as it is the rR allowed symmetric stretch of the Cu-O-Cu core. As shown in Figure 3, all the rR enhanced vibrations of Cu-CHA profile its absorbance feature, which is also inconsistent with a trans- μ -1,2-peroxo species where the CT absorbance feature is made up of three distinct transitions that give different resonance enhancement profiles.³⁵ In another study, the rR features at 1091 cm⁻¹ and 1161 cm⁻¹ were proposed to be O-O stretches of copper superoxide species, ¹⁶ which are commonly observed in this energy region.³⁹ However, if these rR vibrations originated from a different Cu/O species they would not have the same resonance enhancement profile as the symmetric and antisymmetric stretches of the [Cu₂O]²⁺ site and they would also not be formed with N2O. Additionally, copper superoxide species with O-O vibrations in this region generally have $\Delta^{\bar{1}8}O_2$ shifts

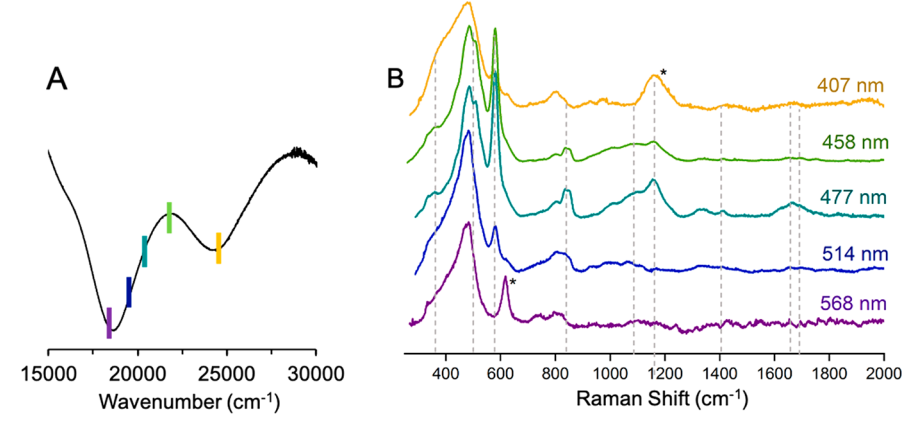


Figure 3. (A) Zoom in of the 22400 cm $^{-1}$ DR UV—vis absorbance feature. (B) Full rR profile of the 22400 cm $^{-1}$ absorption feature formed upon activation with N₂O. Bars on the 22400 cm $^{-1}$ absorbance spectrum in A are the energies of the rR lines used in part B. Dotted lines on the rR spectrum indicate features in resonance with the absorbance feature. (*) indicates features that are not resonantly enhanced by the 22400 cm $^{-1}$ feature but are enhanced by other bands.

around 60 cm⁻¹. Experimentally, we see a smaller value ($\Delta^{18}O_2$ = 32 cm⁻¹) for the $\nu_{2\rm sym}$ vibration at 1,161 cm⁻¹. This is consistent with its assignment as the 2x symmetric stretch which has an experimental value of 581 cm⁻¹ ($\Delta^{(18}O_2)$ = 21 cm⁻¹) and a DFT calculated frequency of 543 cm⁻¹ ($\Delta^{(18}O_2)$ = 10 cm⁻¹) (vide infra).

Three $[Cu_2O]^{2+}$ cores have been previously identified in other zeolite lattices: one in Cu-MFI 10 and two in Cu-MOR. The rR spectra with 458 nm excitation into the ~22000 cm $^{-1}$ absorbance feature of Cu-MFI and Cu-CHA are compared in Figure 4. The rR vibrations of Cu-CHA are shifted compared to those of Cu-MFI. The red highlights in Figure 4 compare the symmetric ($\nu_{\rm sym}$) and 2x symmetric ($\nu_{\rm 2sym}$) stretches of the $[Cu_2O]^{2+}$ cores in Cu-MFI (top) and Cu-CHA (bottom). The $\nu_{\rm sym}$ at 581 cm $^{-1}$ and the $\nu_{\rm 2sym}$ at 1161 cm $^{-1}$ in CHA are both higher in energy than in Cu-MFI ($\nu_{\rm sym}$ at 456 cm $^{-1}$ and $\nu_{\rm 2sym}$ at

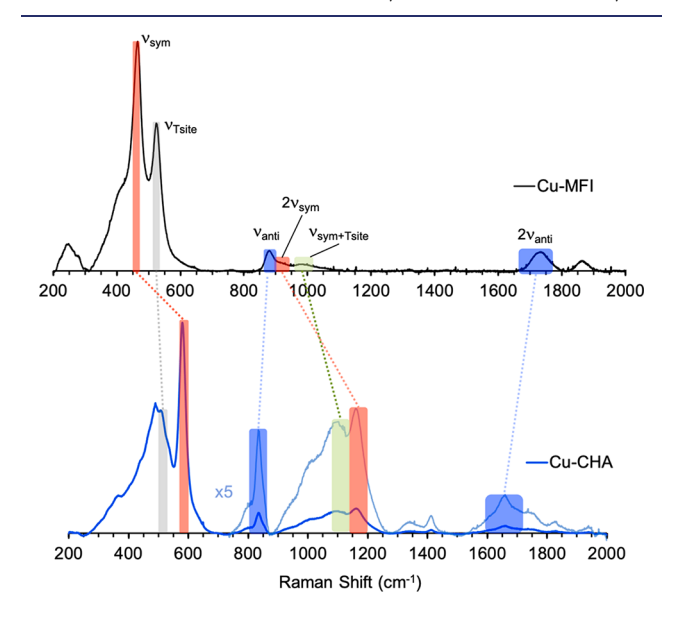


Figure 4. Comparison of the vibrations associated with the $[Cu_2O]^{2+}$ core in Cu-MFI (top) and Cu-CHA (bottom). The symmetric stretches are shown in the red highlights. The antisymmetric stretches are shown in the blue highlights. The T-sites are shown in the gray highlights and the combination band of the T-site + symmetric stretch is shown in the green highlights.

908 cm⁻¹). In contrast, the weaker antisymmetric ($\nu_{\rm anti}$) and the 2x antisymmetric features ($\nu_{\rm 2anti}$) (blue highlights in Figure 4) are shifted to lower energy in Cu-CHA compared to the previously assigned vibrations in Cu-MFI. Interestingly, the T-site resonance enhancement ($\nu_{\rm Tsite}$, gray highlight) in Cu-CHA at 510 cm⁻¹ is located at almost the same energy as the T-site at 514 cm⁻¹ in Cu-MFI. The $\nu_{\rm Tsite}$ + $\nu_{\rm sym}$ combination band also increases in energy from 974 to 1091 cm⁻¹ (green highlight) reflecting the ~120 cm⁻¹ increase in $\nu_{\rm sym}$ for Cu-CHA. A normal coordinate analysis (NCA) of a metaloxygen—metal core was used to correlate the symmetric and antisymmetric vibrations (see Explanation S1) and determined that the Cu-O-Cu angle in Cu-CHA is 120°, compared to ~140° in Cu-MFI and Cu-MOR.

2.4. Kinetic Analysis of the Active Site Reaction with CH₄. The decay of the 22400 cm⁻¹ band of activated Cu-CHA and Cu-MFI was monitored during reaction with methane at a series of temperatures with operando UV—vis spectroscopy to obtain site-selective kinetics of $[Cu_2O]^{2+}$ (see Experimental Section 8 in SI). An Eyring plot was obtained (Figure 5 and Explanation S2), and from the fitted slope and intercept, an enthalpy of activation ΔH^{\ddagger} and entropy of activation ΔS^{\ddagger} were obtained for the $[Cu_2O]^{2+}$ species in Cu-CHA and Cu-MFI (Table 1). The enthalpy barrier is 2.5 kcal/mol lower in Cu-CHA.

2.5. Active Site Models: Comparison to Experiment. Previous studies determined that the [Cu2O]2+ active site in Cu-MFI is stabilized in a 10MR channel, each Cu(II) with bidentate ligation to the oxygens of the Al T-site and a Cu-O-Cu angle of 140°. 10 The CHA lattice does not contain long channels but is made up of cages connected through adjoining 8MR windows (Scheme 2A). Large lattice models (~150 atoms) of both the MFI channel and the CHA cage were optimized using Density Functional Theory (DFT). The model of MFI stabilizes a [Cu₂O]²⁺ core on one side of a 10MR in an O-Al-O-(Si-O)2-Al-O sequence with the oxo of the $[Cu_2O]^{2+}$ site pointed toward the middle of the ring (Figure 6A). Due to the smaller size of the CHA 8MR, a [Cu₂O]²⁺ site with an angle of 120° can only be stabilized across the 8MR and is in an O-Al-O-(Si-O)3-Al-O sequence with the bridging O atom of the [Cu₂O]²⁺ pointing out of the 8MR into a CHA cage (Figure 6B).

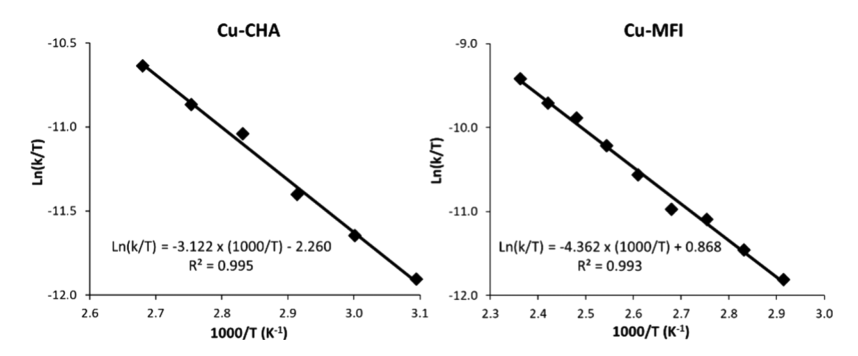


Figure 5. Eyring plot for the reaction of CH₄ with [Cu₂O]²⁺ in Cu-CHA (left) and Cu-MFI (right).

Table 1. Comparison of Kinetic Parameters of the $[Cu_2O]^{2+}$ Species in Cu-CHA and Cu-MFI

	ΔH^{\ddagger} (kcal/mol)	ΔS^{\ddagger} (cal/(mol*K))
CHA	6.2	-51.7
MFI	8.7	-45.5

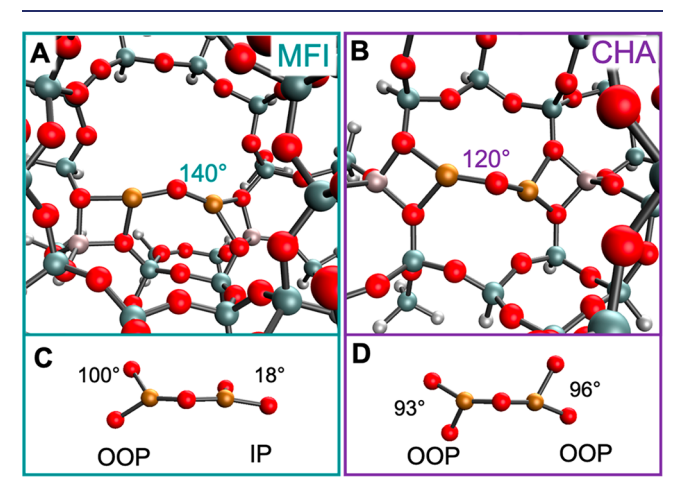


Figure 6. $[Cu_2O]^{2+}$ cores in the MFI (A, green box) and CHA (B, purple box) lattices and schematic of bidentate oxygen ligation of $[Cu_2O]^{2+}$ cores in MFI (C) and CHA (D) assigning out of plane (OOP) and in plane (IP) ligation with respect to the Cu–O–Cu plane.

Note that the $[Cu_2O]^{2+}$ active sites identified in CHA and MFI also differ in their bidentate coordination to the lattice oxygens of the Al T-site. In CHA, the oxygen atoms of both bidentate T-site ligands are oriented out of the Cu–O–Cu plane by 93° and 96° (Figure 6D). In contrast, in MFI one set of bidentate lattice oxygens is more in the Cu–O–Cu plane (IP) (18°) and one set is out of plane (OOP) (100°) (Figure 6).

A comparison of the experimental and DFT predicted $[Cu_2O]^{2+}$ structures and spectroscopic features for both lattices are presented in Table 2. The calculated angles of the $[Cu_2O]^{2+}$ cores are in good agreement with the experimental values determined by rR and NCA (Explanation S1) (139.5° vs 140° for MFI; 126° vs 120° for CHA). The calculated Cu–O–Cu symmetric and antisymmetric vibrations as well as their $\Delta^{18}O_2$ shifts reinforce the experimental assignments.

2.6. Reaction Coordinate Calculations. To elucidate the origin of the higher experimental reactivity of methane with the active site in Cu-CHA compared to Cu-MFI (Table 1), the H atom abstraction (HAA) reaction coordinates of CH₄ to form

Table 2. Comparison of Experimental and Predicted Spectroscopic and Structural Features of MFI and CHA and Their Corresponding Large Models

	MFI (Exp)	MFI Channel	CHA (Exp)	CHA Cage
∠ Cu−O−Cu/°	140	140	120	126
$d(Cu-O_{lattice})/Å$		1.98 - 2.04		1.93-2.04
$d(Cu-O_{oxo})/Å$		1.75		1.73-1.75
Abs/cm ⁻¹	22700	24930	22000	23246/26099
$v_{\text{sym}} \frac{(\Delta^{18} O_2)}{\text{cm}^{-1}}$	456 (8)	454 (5)	580 (21)	543 (10)
$v_{\underset{\hbox{cm}}{\text{asym}}} (\Delta^{18} \text{O}_2) /$	870 (40)	847 (41)	837 (43)	842 (40.5)

 $[Cu_2OH]^{2+}$ and a ·CH₃ radical were calculated for the large lattice models, both with dispersion (solid lines) and with the dispersion removed (dotted lines) (Figure 7). The correspond-

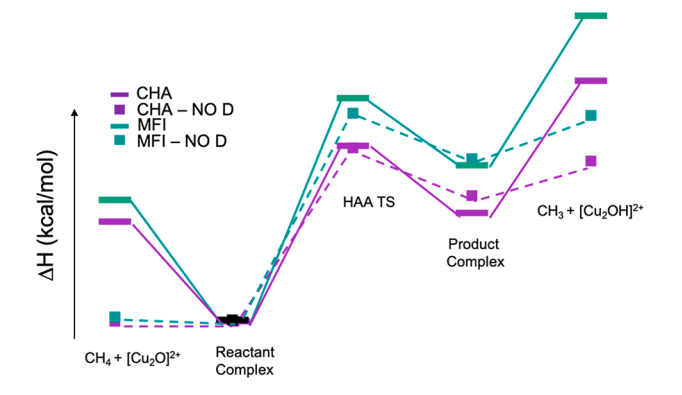


Figure 7. $\mathrm{CH_4}$ reaction coordinates for large channel/cage models for MFI (green) and CHA (purple). Dotted lines are calculations without dispersion. Values for each step in the reaction coordinate for each structure are given in Table 3. Reactant Complex energies are all set to zero.

ing enthalpy values are given in Table 3. The difference between the calculations with and without dispersion gives an estimate of the physisorption contribution to the energetics of each step. The sites were optimized with dispersion, then the structure was fixed, and the dispersion was eliminated. Starting from the left of the reaction coordinate in Figure 7, gas phase methane is first physisorbed to the Cu–O–Cu active site (Reactant Complex, RC). The RC then goes through a transition state (TS) to form a product complex (PC) which is a Cu $^{\rm I}$ –OH–Cu $^{\rm II}$ core with a physisorbed \cdot CH $_3$ radical. The \cdot CH $_3$ radical was then removed from the zeolite lattice to

Table 3. Enthalpy Values (kcal/mol) for the Different Complexes in Figure 7

	no dispersion		dispersion	
ΔH (kcal/mol)	CHA Cage	MFI Channel	CHA Cage	MFI Channel
CH ₄ + [Cu ₂ O] ²⁺	0.0	0.4	9.5	11.7
Reactant Complex	0.0	0.0	0.0	0.0
HAA Transition State	16.6	19.9	16.9	21.3
Product Complex	12.0	15.6	10.3	15.0
CH ₃ + [Cu ₂ OH] ²⁺	15.4	19.8	23.0	29.2

calculate the physisorption contribution to the energetics of the product complex.

Physisorption of CH₄ into the zeolite lattice was evaluated to determine its effect on the apparent activation barrier. Relative to the calculations without dispersion, methane physisorption from the gas phase to the active site is favorable by ~10 kcal/ mol (Figure 7, left to RC). There is not much difference in the physisorption energetics between the CHA and MFI models, suggesting that this does not contribute to the increased reactivity in CHA. This is in contrast to the results in MOR where the physisorption energy difference was the dominating contribution to the difference in reactivity between a more and a less confined [Cu₂O]²⁺ species.²⁵ On the right side of Figure 7, physisorption of the methyl radical to the Cu-OH-Cu product (Figure 7, right to PC) is calculated to be favorable by ~10 kcal/mol. There is an additional interaction of the new Hbond formed between the methyl radical and the Cu-OH-Cu core that results from the HAA reaction that is worth ~3 kcal/ mol (based on the stabilization of the CH3 radical by the [Cu₂OH]²⁺ site without dispersion). Overall, the models exhibit similar physisorption into the zeolite for both the CH₄ substrate and the ·CH3 radical.

Now focusing on the TS energies, CHA has a 4.4 kcal/mol lower TS energy compared to MFI (CHA lower by 3.3 kcal/ mol in the calculations without dispersion). If we look at apparent values where we compare the $CH_4 + [Cu_2O]^{2+}$ to the HAA TS, the difference is 2.2 kcal/mol with dispersion. This value is in good agreement with the experimental enthalpy difference with CHA lower than MFI by 2.5 kcal/mol (Table 1). In order to determine the effect of thermodynamics on the TS, Marcus theory⁴¹ was used to extract the intrinsic barriers (i.e., with no thermodynamic driving force; see Explanation S3). These values are given in Table 4. The calculated intrinsic barriers for the Cu-CHA and Cu-MFI reaction coordinates in the large lattice models are similar (11.2 vs 12.7 kcal/mol) indicating that most of the 4.4 kcal/mol of TS difference is due to the thermodynamic difference between the reactant and the product.

Table 4. HAA Transition State energies (kcal/mol), Marcus Corrected Intrinsic Barriers, and Calculated O–H Bond Strengths for Large Lattice Models^a

ΔH (kcal/mol)	HAA Transition State	Intrinsic Barrier	OH Bond Strength
CHA CAGE	16.9	11.2	89.8
MFI Channel	21.3	12.7	85.8

^aWith respect to the 103.3 kcal/mol calculated C-H bond of CH₄.

The difference in energy of the two extremes on the reaction coordinate in Figure 7 (where the $\mathrm{CH_4}$ and $\cdot\mathrm{CH_3}$ are in the gas phase removed from the active site cores) gives direct insight into the thermodynamics for the reaction coordinate, reflecting the strength of the O–H bond formed along the HAA reaction coordinate (values are given in Table 4). The O–H bond formed in Cu-CHA is calculated to be 4 kcal/mol stronger than MFI. Therefore, the higher reactivity exhibited in Cu-CHA is due to the stronger O–H bond that forms in Cu-CHA. We also calculated HAA reaction coordinates for small ring models (SRMs) that do not include the walls of the zeolite lattice. These SRMs reproduce the trends observed in the large lattice models (Explanation S4).

To determine the geometric and electronic structure contributions to this OH bond strength difference between CHA and MFI, smaller models were developed by extracting the Cu–O–Cu reactant and Cu–OH–Cu product cores along with their coordinating O–Al–O T-sites from the large lattice models (Figure 8). The lattice Si atoms capping the Al T-sites

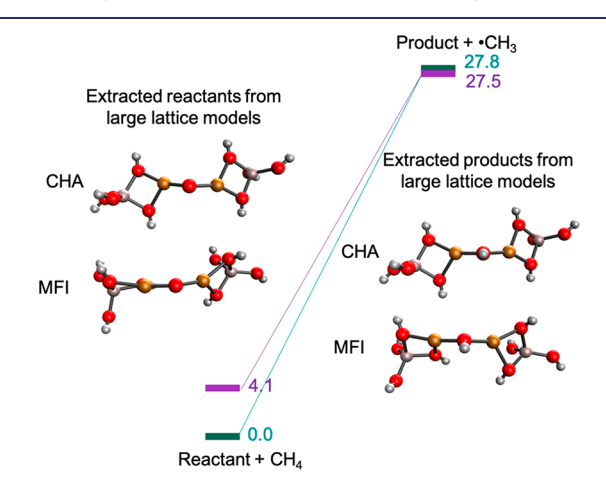


Figure 8. Relative stability of extracted Cu-O-Cu reactant and Cu-OH-Cu product cores for MFI (green) and CHA (purple).

were replaced with hydrogen atoms set along the bond direction to a bond length of 0.96 Å. To ensure that the small core model had the same coordinates (angles, bond lengths, bidentate O angles, etc.) as the larger lattice models, no additional optimization was performed after extracting the core and capping the Al T-sites with hydrogens. A single point calculation was performed to obtain the energy of each structure. These extracted core models of MFI and CHA have the same number of atoms and electrons and can be directly compared (Figure 8).

The reactant Cu-O-Cu core in Cu-CHA was calculated to be 4.1 kcal/mol higher in energy than that in Cu-MFI while the Cu-OH-Cu product was calculated to be only 0.3 kcal/mol higher in Cu-CHA than in Cu-MFI. This indicates that the higher OH bond strength in CHA derives from a destabilization of the reactant Cu-O-Cu core imposed by the CHA lattice.

As mentioned earlier in the study, the main structural differences between the reactant cores of CHA and MFI are the angles of the Cu–O–Cu core (120° in MFI and 140° in CHA) and the rotations of the bidentate oxygen ligands with respect to the Cu–O–Cu plane (close to $90^{\circ}/0^{\circ}$ in MFI and $90^{\circ}/90^{\circ}$ in CHA). The contributions of these differences to the relative destabilization of 4.1 kcal/mol of the reactant core

in CHA were evaluated using a series of small models (Experimental Section 10 in SI). A series of fixed ligand rotations was evaluated $(0^{\circ}/0^{\circ}, 90^{\circ}/0^{\circ}, +45^{\circ}/-45^{\circ}, \text{ and } 90^{\circ}/90^{\circ})$ with respect to the Cu–O–Cu plane. These ligand rotation sets were analyzed for three Cu–O–Cu angles (161° from unconstrained optimization, 140° to reflect MFI, and 120° to reflect CHA). The relative energies for these models are given in Table 5 and their structure and LUMOs in Figure

Table 5. Comparison of Energies (kcal/mol) of Models with Various Cu-O-Cu Angles and Bidentate Oxygen Ligand Rotation

Energy (kcal/mol)		Cu-O-Cu angle	
Bidentate Oxygen Ligand Rotations (with respect to the Cu–O–Cu plane)	161°	140°	120°
+45°/-45°	0.4	1.4	0.2
0°/0°	6.4	7.2	14.5 ^a
90°/0°	0.0	2.5	0.3
90°/90°	6.7	5.5	5.9

"larger energy difference due to steric interaction between two in plane Al T ligands at the acute 120° angle.

S14. Table 5 shows that for models with the same bidentate oxygen ligand rotations, the Cu–O–Cu angle does not significantly affect the energy. The models with the two bidentate oxygen pairs in the same plane as each other (rotated $0^{\circ}/0^{\circ}$ and $90^{\circ}/90^{\circ}$ with respect to the Cu–O–Cu plane) are calculated to be ~6 kcal/mol higher in energy than those with ligand sets rotated by 90° from each other (rotated $+45^{\circ}/-45^{\circ}$ and $90^{\circ}/0^{\circ}$ with respect to the Cu–O–Cu plane) across all evaluated Cu–O–Cu angles. The relative rotation of the bidentate ligands with respect to each other significantly impacts the energy, however the rotation of the bidentate ligands with respect to the Cu-O-Cu does not.

The bidentate O–Al–O T-site ligation on each Cu results in a highest energy singly occupied d x^2 - y^2 orbital on each metal. The $[Cu_2O]^{2+}$ models with the bidentate oxygen ligands in the same plane as each other (Figure 9, right) have two frontier molecular orbitals (FMOs) (the β LUMO and β LUMO+1) that are the (–) and (+) combinations, respectively, of the d x^2 - y^2 orbitals on each Cu(II), delocalized over the model. The (+) combination (Figure 9, top right) of the two Cu d x^2 - y^2

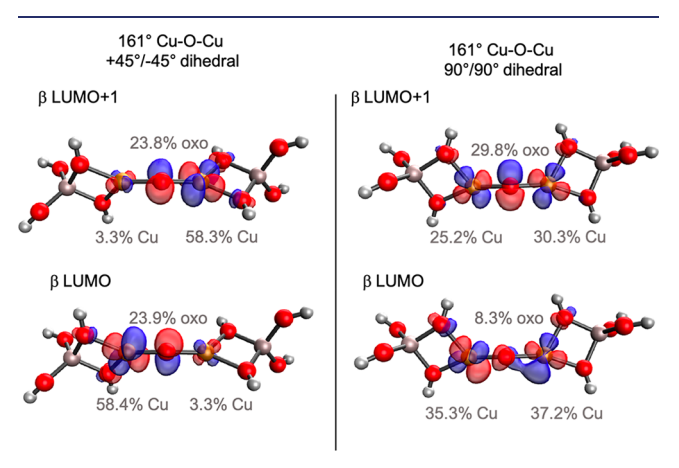


Figure 9. Comparison of FMOs for bidentate oxygen ligands rotated 90° from each other (left) and in the same plane (right) (triplet ground state; see SI Figure S13 for the full series).

orbitals interacts with an OOP oxo 2p orbital leading to 29.8% oxo character while the (-) combination (Figure 9, bottom right) has only a limited interaction with the IP oxo 2p orbital and thus a small amount (8.3%) of oxo character. In the models with ligand sets rotated 90° from each other, the two FMOs are again (+) and (-) combinations of d x^2 -y² orbitals but now each is localized on a different Cu(II) which interacts with a different oxo p orbital, resulting in \sim 24% oxo character for both combinations (Figure 9, left).

Thus, for the ligand sets with 90° relative rotation as in MFI, each Cu d x^2 - y^2 orbital has a strong bonding interaction with a different oxo p orbital resulting in 10% more oxo character distributed over the two LUMOs relative to the 0° ligand rotation in Figure 9 (right) (47.7% vs 38.1% total oxo character). This results in the stabilization of this active site relative to the 0° rotation as in CHA, where each Cu d x^2 - y^2 orbital competes with the same oxo 2p orbital for bonding. Thus, the copper atoms in CHA bind less strongly to the oxo than those in MFI destabilizing the $[Cu_2O]^{2+}$ active site and priming it for reactivity. This conclusion holds throughout the series of small models with varying Cu–O–Cu angles in Figure S14.

3. DISCUSSION

A [Cu₂O]²⁺ core with an angle of 120° is identified as the active site in Cu-CHA that converts methane to methanol at low temperature. This [Cu₂O]²⁺ active site assignment in Cu-CHA is different from previous proposals of multiple Cu/O species contributing to the features observed in the Cu-CHA rR spectrum. 15,16 These previous assignments were largely based on empirical correlations to Cu/O structures present in model and enzyme literature. 10,35,42,43 However, in the present study, additional new data were collected including the rR spectrum of Cu-CHA activated with N₂O, the ¹⁸O₂ perturbation on the rR spectrum, the full resonance enhancement profile over the associated absorption feature, and an extension of the rR spectrum to the higher energy overtone region. These additional experiments enabled an unambiguous assignment of the rR features of Cu-CHA, highlighting the importance of rigorous spectroscopy and the possibility of inaccurate assignments relying on empirical correlations to define an intermediate.

From rR, the $[Cu_2O]^{2+}$ site defined in Cu-CHA has a more acute Cu-O-Cu angle than the one defined in Cu-MFI and, from kinetic experiments, is found to have a lower enthalpic barrier by 2.5 kcal/mol. DFT modeling reproduces the experimental results and indicates that this difference in reactivity is due to the thermodynamic driving force associated with the stronger O-H bond formed in the $[Cu_2OH]^{2+}$ CHA intermediate generated in the HAA reaction. While the $[Cu_2OH]^{2+}$ intermediates in the two lattices are similar in energy, the reactant $[Cu_2O]^{2+}$ site in Cu-CHA is destabilized compared to that in Cu-MFI and this lowers the activation barrier in Cu-CHA. This destabilization is not due to the change in the Cu-O-Cu angle but derives from the lattice-imposed relative orientations of the two bidentate oxygen ligand sets.

The results from the present study on Cu-CHA and Cu-MFI are different from what was found in our prior studies on Cu-MOR where two $[Cu_2O]^{2+}$ sites are present with different reactivity but similar Cu-O-Cu structures.²⁵ In MOR, the two $[Cu_2O]^{2+}$ sites are located in different parts of the zeolite lattice: one in the constrained 8MR side pocket and one in a

large 12MR channel. Their difference in the apparent activation is due to the large difference in physisorption enthalpy for the two sites ($\Delta \Delta H = 7.7 \text{ kcal/mol}$) reflecting stabilization by the constrained pocket. In the present study, physisorption was calculated to be similar in both CHA and MFI (Figure 7, left side) and it is not a dominating contribution to the difference in apparent activation barriers between CHA and MFI. The lattice constraints associated with the bidentate T-site ligation in CHA impose a destabilizing geometry on the [Cu-O-Cu]²⁺ core, reminiscent of the entatic state in metalloproteins where protein constraints enforce an unstable geometry that is associated with high reactivity. It is interesting to note that the approximate perpendicular orientation of the bidentate O-Al-O T-Site ligand planes in MFI and their parallel orientation in CHA would reflect the lower and upper limits on this role of the zeolite lattice in activating a [Cu₂O]²⁺ core. Improvement upon the reactivity of [Cu₂O]²⁺ in Cu-CHA could occur via topologies with a more confined cage which still maintains coplanar geometry of the four lattice oxygen ligands. The latter depends not only on the zeolite topology but also on the location of Al substitution which can, in some cases, be guided during the zeolite synthesis.44-46

Together, the previous study on MOR and the present study demonstrate two means through which a carefully chosen zeolite support can enhance the reactivity of a $[Cu_2O]^{2+}$ species, providing a direction for optimization toward room temperature reactivity. This would open up new applications for these materials, such as the ambient capturing of CH_4 from dilute emission streams or from the atmosphere as a negative emission technology. ¹⁹

ASSOCIATED CONTENT

Supporting Information

The Supporting Information is available free of charge at https://pubs.acs.org/doi/10.1021/jacs.1c02835.

Experimental section, PXRD patterns, nitrogen sorption isotherms, additional DR UV—vis spectra and rR spectra of Cu-CHA, rR of ¹⁸O₂ activated Cu-CHA, normal coordinate analysis of a Cu–O—Cu angle, Arrhenius plot of the reaction of CH₄ with Cu-CHA and Cu-MFI, DFT of small ring Cu-CHA and Cu-MFI models, DFT cluster model coordinates (PDF)

AUTHOR INFORMATION

Corresponding Authors

Robert A. Schoonheydt — Department of Microbial and Molecular Systems, Center for Sustainable Catalysis and Engineering, KU Leuven, B-3001 Leuven, Belgium; Email: robert.schoonheydt@kuleuven.be

Bert F. Sels – Department of Microbial and Molecular Systems, Center for Sustainable Catalysis and Engineering, KU Leuven, B-3001 Leuven, Belgium; orcid.org/0000-0001-9657-1710; Email: bert.sels@kuleuven.be

Edward I. Solomon — Department of Chemistry, Stanford University, Stanford, California 94305, United States; Photon Science, SLAC National Accelerator Laboratory, Menlo Park, California 94025, United States; orcid.org/0000-0003-0291-3199; Email: edward.solomon@stanford.edu

Authors

Hannah M. Rhoda — Department of Chemistry, Stanford University, Stanford, California 94305, United States; orcid.org/0000-0001-5730-5209

Dieter Plessers – Department of Microbial and Molecular Systems, Center for Sustainable Catalysis and Engineering, KU Leuven, B-3001 Leuven, Belgium

Alexander J. Heyer — Department of Chemistry, Stanford University, Stanford, California 94305, United States; orcid.org/0000-0003-4362-8191

Max L. Bols – Department of Microbial and Molecular Systems, Center for Sustainable Catalysis and Engineering, KU Leuven, B-3001 Leuven, Belgium; orcid.org/0000-0002-4576-5969

Complete contact information is available at: https://pubs.acs.org/10.1021/jacs.1c02835

Author Contributions

\$These authors contributed equally to this work

Notes

The authors declare no competing financial interest.

ACKNOWLEDGMENTS

Funding for this work was provided by National Science Foundation Grant CHE-1660611(to E.I.S.), the Stanford Woods Institute for the Environment, and the National Institutes of Health Grant R01DK031450 (to E.I.S.). Research Foundation — Flanders is acknowledged for grant G0A2216N (to B.F.S.), 11D4718N (to D.P.) and 1276021N (to M.B.). We thank SACHEM for providing the TMAdaOH organic structure directing agent.

REFERENCES

- (1) Snyder, B. E. R.; Bols, M. L.; Schoonheydt, R. A.; Sels, B. F.; Solomon, E. I. Iron and Copper Active Sites in Zeolites and Their Correlation to Metalloenzymes. *Chem. Rev.* **2018**, *118*, 2718–2768.
- (2) Hammond, C.; Conrad, S.; Hermans, I. Oxidative Methane Upgrading. ChemSusChem 2012, 5, 1668–1686.
- (3) Banerjee, R.; Proshlyakov, Y.; Lipscomb, J. D.; Proshlyakov, D. A. Structure of the Key Species in the Enzymatic Oxidation of Methane to Methanol. *Nature* **2015**, *518*, 431–434.
- (4) Castillo, R. G.; Banerjee, R.; Allpress, C. J.; Rohde, G. T.; Bill, E.; Que, L.; Lipscomb, J. D.; DeBeer, S. High-Energy-Resolution Fluorescence-Detected X-Ray Absorption of the Q Intermediate of Soluble Methane Monooxygenase. *J. Am. Chem. Soc.* **2017**, *139*, 18024—18033.
- (5) Cutsail, G. E.; Banerjee, R.; Zhou, A.; Que, L.; Lipscomb, J. D.; DeBeer, S. High-Resolution Extended X-Ray Absorption Fine Structure Analysis Provides Evidence for a Longer Fe···Fe Distance in the Q Intermediate of Methane Monooxygenase. *J. Am. Chem. Soc.* **2018**, *140*, 16807–16820.
- (6) Culpepper, M. A.; Rosenzweig, A. C. Architecture and Active Site of Particulate Methane Monooxygenase. *Crit. Rev. Biochem. Mol. Biol.* **2012**, 47, 483–492.
- (7) Ross, M. O.; MacMillan, F.; Wang, J.; Nisthal, A.; Lawton, T. J.; Olafson, B. D.; Mayo, S. L.; Rosenzweig, A. C.; Hoffman, B. M. Particulate Methane Monooxygenase Contains Only Mononuclear Copper Centers. *Science* **2019**, *364*, 566–570.
- (8) Vanelderen, P.; Snyder, B. E. R.; Tsai, M.-L.; Hadt, R. G.; Vancauwenbergh, J.; Coussens, O.; Schoonheydt, R. A.; Sels, B. F.; Solomon, E. I. Spectroscopic Definition of the Copper Active Sites in Mordenite: Selective Methane Oxidation. *J. Am. Chem. Soc.* **2015**, 137, 6383–6392.
- (9) Snyder, B. E. R.; Vanelderen, P.; Bols, M. L.; Hallaert, S. D.; Böttger, L. H.; Ungur, L.; Pierloot, K.; Schoonheydt, R. A.; Sels, B. F.;

- Solomon, E. I. The Active Site of Low-Temperature Methane Hydroxylation in Iron-Containing Zeolites. *Nature* **2016**, *536*, 317–321.
- (10) Woertink, J. S.; Smeets, P. J.; Groothaert, M. H.; Vance, M. A.; Sels, B. F.; Schoonheydt, R. A.; Solomon, E. I. A [Cu 2 O] 2+ Core in Cu-ZSM-5, the Active Site in the Oxidation of Methane to Methanol. *Proc. Natl. Acad. Sci. U. S. A.* **2009**, *106*, 18908–18913.
- (11) Dinh, K. T.; Sullivan, M. M.; Serna, P.; Meyer, R. J.; Dincă, M.; Román-Leshkov, Y. Viewpoint on the Partial Oxidation of Methane to Methanol Using Cu- and Fe-Exchanged Zeolites. *ACS Catal.* **2018**, *8*, 8306–8313.
- (12) Newton, M. A.; Knorpp, A. J.; Sushkevich, V. L.; Palagin, D.; van Bokhoven, J. A. Active Sites and Mechanisms in the Direct Conversion of Methane to Methanol Using Cu in Zeolitic Hosts: A Critical Examination. *Chem. Soc. Rev.* **2020**, *49*, 1449–1486.
- (13) Snyder, B. E. R.; Böttger, L. H.; Bols, M. L.; Yan, J. J.; Rhoda, H. M.; Jacobs, A. B.; Hu, M. Y.; Zhao, J.; Alp, E. E.; Hedman, B.; Hodgson, K. O.; Schoonheydt, R. A.; Sels, B. F.; Solomon, E. I. Structural Characterization of a Non-Heme Iron Active Site in Zeolites That Hydroxylates Methane. *Proc. Natl. Acad. Sci. U. S. A.* **2018**, *115*, 4565–4570.
- (14) Tabor, E.; Dedecek, J.; Mlekodaj, K.; Sobalik, Z.; Andrikopoulos, P. C.; Sklenak, S. Dioxygen Dissociation over Man-Made System at Room Temperature to Form the Active α -Oxygen for Methane Oxidation. *Sci. Adv.* **2020**, *6*, 1–9.
- (15) Ipek, B.; Wulfers, M. J.; Kim, H.; Göltl, F.; Hermans, I.; Smith, J. P.; Booksh, K. S.; Brown, C. M.; Lobo, R. F. Formation of [Cu 2 O 2] 2+ and [Cu 2 O] 2+ toward C-H Bond Activation in Cu-SSZ-13 and Cu-SSZ-39. ACS Catal. 2017, 7, 4291–4303.
- (16) Pappas, D. K.; Borfecchia, E.; Dyballa, M.; Pankin, I. A.; Lomachenko, K. A.; Martini, A.; Signorile, M.; Teketel, S.; Arstad, B.; Berlier, G.; Lamberti, C.; Bordiga, S.; Olsbye, U.; Lillerud, K. P.; Svelle, S.; Beato, P. Methane to Methanol: Structure—Activity Relationships for Cu-CHA. *J. Am. Chem. Soc.* **2017**, *139*, 14961—14975.
- (17) Grundner, S.; Markovits, M. A. C.; Li, G.; Tromp, M.; Pidko, E. A.; Hensen, E. J. M.; Jentys, A.; Sanchez-Sanchez, M.; Lercher, J. A. Single-Site Trinuclear Copper Oxygen Clusters in Mordenite for Selective Conversion of Methane to Methanol. *Nat. Commun.* **2015**, *6*, 7546.
- (18) Tomkins, P.; Mansouri, A.; Bozbag, S. E.; Krumeich, F.; Park, M. B.; Alayon, E. M. C.; Ranocchiari, M.; van Bokhoven, J. A. Isothermal Cyclic Conversion of Methane into Methanol over Copper-Exchanged Zeolite at Low Temperature. *Angew. Chem., Int. Ed.* **2016**, *55*, 5467–5471.
- (19) Jackson, R. B.; Solomon, E. I.; Canadell, J. G.; Cargnello, M.; Field, C. B. Methane Removal and Atmospheric Restoration. *Nat. Sustain.* **2019**, *2*, 436–438.
- (20) Xin, Y.; Li, Q.; Zhang, Z. Zeolitic Materials for DeNO _x Selective Catalytic Reduction. *ChemCatChem* **2018**, *10*, 29–41.
- (21) Zhang, R.; Liu, N.; Lei, Z.; Chen, B. Selective Transformation of Various Nitrogen-Containing Exhaust Gases toward N ₂ over Zeolite Catalysts. *Chem. Rev.* **2016**, *116*, 3658–3721.
- (22) Beale, A. M.; Gao, F.; Lezcano-Gonzalez, I.; Peden, C. H. F.; Szanyi, J. Recent Advances in Automotive Catalysis for NO $_{\rm x}$ Emission Control by Small-Pore Microporous Materials. *Chem. Soc. Rev.* 2015, 44, 7371–7405.
- (23) Borfecchia, E.; Beato, P.; Svelle, S.; Olsbye, U.; Lamberti, C.; Bordiga, S. Cu-CHA a Model System for Applied Selective Redox Catalysis. *Chem. Soc. Rev.* **2018**, *47*, 8097–8133.
- (24) Ipek, B.; Lobo, R. F. Catalytic Conversion of Methane to Methanol on Cu-SSZ-13 Using N 2 O as Oxidant. *Chem. Commun.* **2016**, *52*, 13401–13404.
- (25) Snyder, B. E. R.; Vanelderen, P.; Schoonheydt, R. A.; Sels, B. F.; Solomon, E. I. Second-Sphere Effects on Methane Hydroxylation in Cu-Zeolites. *J. Am. Chem. Soc.* **2018**, *140*, 9236–9243.
- (26) Negri, C.; Signorile, M.; Porcaro, N. G.; Borfecchia, E.; Berlier, G.; Janssens, T. V. W.; Bordiga, S. Dynamic CuII/CuI Speciation in

- Cu-CHA Catalysts by in Situ Diffuse Reflectance UV-Vis-NIR Spectroscopy. *Appl. Catal., A* **2019**, 578, 1-9.
- (27) Oord, R.; Schmidt, J. E.; Weckhuysen, B. M. Methane-to-Methanol Conversion over Zeolite Cu-SSZ-13, and Its Comparison with the Selective Catalytic Reduction of NOx with NH3. *Catal. Sci. Technol.* **2018**, *8*, 1028–1038.
- (28) Giordanino, F.; Vennestrøm, P. N. R.; Lundegaard, L. F.; Stappen, F. N.; Mossin, S.; Beato, P.; Bordiga, S.; Lamberti, C. Characterization of Cu-Exchanged SSZ-13: A Comparative FTIR, UV-Vis, and EPR Study with Cu-ZSM-5 and Cu- β with Similar Si/Al and Cu/Al Ratios. *Dalt. Trans.* **2013**, *42*, 12741–12761.
- (29) Godiksen, A.; Stappen, F. N.; Vennestrøm, P. N. R.; Giordanino, F.; Rasmussen, S. B.; Lundegaard, L. F.; Mossin, S. Coordination Environment of Copper Sites in Cu-CHA Zeolite Investigated by Electron Paramagnetic Resonance. *J. Phys. Chem. C* **2014**, *118*, 23126–23138.
- (30) Li, H.; Paolucci, C.; Khurana, I.; Wilcox, L. N.; Göltl, F.; Albarracin-Caballero, J. D.; Shih, A. J.; Ribeiro, F. H.; Gounder, R.; Schneider, W. F. Consequences of Exchange-Site Heterogeneity and Dynamics on the UV-Visible Spectrum of Cu-Exchanged SSZ-13. *Chem. Sci.* **2019**, *10*, 2373–2384.
- (31) Wulfers, M. J.; Teketel, S.; Ipek, B.; Lobo, R. F. Conversion of Methane to Methanol on Copper-Containing Small-Pore Zeolites and Zeotypes. *Chem. Commun.* **2015**, *51*, 4447–4450.
- (32) Beznis, N. V.; Weckhuysen, B. M.; Bitter, J. H. Cu-ZSM-5 Zeolites for the Formation of Methanol from Methane and Oxygen: Probing the Active Sites and Spectator Species. *Catal. Lett.* **2010**, *138*, 14–22.
- (33) Sushkevich, V. L.; Palagin, D.; Ranocchiari, M.; van Bokhoven, J. A. Selective Anaerobic Oxidation of Methane Enables Direct Synthesis of Methanol. *Science* **2017**, *356*, 523–527.
- (34) Brezicki, G.; Kammert, J. D.; Gunnoe, T. B.; Paolucci, C.; Davis, R. J. Insights into the Speciation of Cu in the Cu-H-Mordenite Catalyst for the Oxidation of Methane to Methanol. *ACS Catal.* **2019**, 9, 5308–5319.
- (35) Baldwin, M. J.; Ross, P. K.; Pate, J. E.; Tyeklar, Z.; Karlin, K. D.; Solomon, E. I.; Tyeklàr, Z.; Karlin, K. D.; Solomon, E. I.; Pate, J. E.; Tyeklàr, Z.; Karlin, K. D. Spectroscopic and Theoretical Studies of an End-on Peroxide-Bridged Coupled Binuclear Copper(II) Model Complex of Relevance to the Active Sites in Hemocyanin and Tyrosinase. J. Am. Chem. Soc. 1991, 113, 8671–8679.
- (36) Brunold, T. C.; Tamura, N.; Kitajima, N.; Moro-oka, Y.; Solomon, E. I. Spectroscopic Study of [Fe 2 (O 2)(OBz) 2 {HB(Pz') 3 } 2]: Nature of the μ -1,2 Peroxide–Fe(III) Bond and Its Possible Relevance to O 2 Activation by Non-Heme Iron Enzymes. *J. Am. Chem. Soc.* **1998**, 120, 5674–5690.
- (37) Li, L.; Solomon, E. I.; Lucas, H. R.; Karlin, K. D.; Sarjeant, A. A. N.; Vance, M. A. Toluene and Ethylbenzene Aliphatic C–H Bond Oxidations Initiated by a Dicopper(II)-μ-1,2-Peroxo Complex. *J. Am. Chem. Soc.* **2009**, *131*, 3230–3245.
- (38) Lee, Y.; Park, G. Y.; Lucas, H. R.; Vajda, P. L.; Kamaraj, K.; Vance, M. A.; Milligan, A. E.; Woertink, J. S.; Slegler, M. A.; Narducci Sarjeant, A. A.; Zakharov, L. N.; Rheingold, A. L.; Solomon, E. I.; Karlin, K. D. Copper(I)/O2 Chemistry with Imidazole Containing Tripodal Tetradentate Ligands Leading to μ-1,2-Peroxo-Dicopper(II) Species. *Inorg. Chem.* **2009**, *48*, 11297–11309.
- (39) Maiti, D.; Fry, H. C.; Woertink, J. S.; Vance, M. A.; Solomon, E. I.; Karlin, K. D. A 1:1 Copper-Dioxygen Adduct Is an End-on Bound Superoxo Copper(II) Complex Which Undergoes Oxygenation Reactions with Phenols. J. Am. Chem. Soc. 2007, 129, 264–265.
- (40) Wing, R. M.; Callahan, K. P. Characterization of Metal-Oxygen Bridge Systems. *Inorg. Chem.* **1969**, *8*, 871–874.
- (41) Marcus, R. A. Theoretical Relations among Rate Constants, Barriers, and Bronsted Slopes of Chemical Reactions. *J. Phys. Chem.* **1968**, 72, 891–899.
- (42) Mirica, L. M.; Ottenwaelder, X.; Stack, T. D. P. Structure and Spectroscopy of Copper–Dioxygen Complexes. *Chem. Rev.* **2004**, 104, 1013–1046.

- (43) Baldwin, M. J.; Roo, D. E.; Pate, J. E.; Fujisawa, K.; Kitajima, N.; Solomon, E. I. Spectroscopic Studies of Side-On Peroxide-Bridged Binuclear Copper(II) Model Complexes of Relevance to Oxyhemocyanin and Oxytyrosinase. *J. Am. Chem. Soc.* **1992**, *114*, 10421–10431.
- (44) Di Iorio, J. R.; Gounder, R. Controlling the Isolation and Pairing of Aluminum in Chabazite Zeolites Using Mixtures of Organic and Inorganic Structure-Directing Agents. *Chem. Mater.* **2016**, 28, 2236–2247.
- (45) Devos, J.; Bols, M. L.; Plessers, D.; Goethem, C.; Van; Seo, J. W.; Hwang, S. J.; Sels, B. F.; Dusselier, M. Synthesis-Structure-Activity Relations in Fe-CHA for C-H Activation: Control of Al Distribution by Interzeolite Conversion. *Chem. Mater.* **2020**, 32, 273–285.
- (46) Di Iorio, J. R.; Nimlos, C. T.; Gounder, R. Introducing Catalytic Diversity into Single-Site Chabazite Zeolites of Fixed Composition via Synthetic Control of Active Site Proximity. *ACS Catal.* **2017**, *7*, 6663–6674.